

光学学报

基于毫米级 Au 红外辐射抑制超材料的设计与制备

李晨曦, 李享成*, 陈平安, 朱颖丽, 朱伯铨

武汉科技大学省部共建耐火材料与冶金国家重点实验室, 湖北 武汉 430081

摘要 基于时域有限差分法仿真模拟了毫米级超材料的中远红外光谱响应,并结合电场散射效应分析了毫米方形图案的边缘电场分布对红外反射率的影响。通过参数扫描法优化得到了方形单元的最优厚度。将边缘区域离散化为独立单元,并将 x, y 方向分别设置为完美匹配层(PML)、periodic 边界条件,通过迭代计算及加权叠加获得了毫米方形超材料的红外光谱响应及电场分布。结果表明,该超材料在 $2\sim 16\ \mu\text{m}$ 内的红外反射率保持在 81.9% 以上,最高可达 87.05%。当图案占空比相同时,单元周期的减小增强了超材料边缘区域的电场散射效应,导致其在 $8\sim 10\ \mu\text{m}$ 远红外波段内的反射率保持在 84.25% 以上。实测结果与仿真结果较好地吻合,这为毫米级红外辐射抑制超材料的设计提供了新的思路。

关键词 光学设计; 毫米级超材料; 电场散射效应; 时域有限差分法; 中远红外高反射

中图分类号 TN213

文献标志码 A

DOI: 10.3788/AOS231471

1 引言

红外辐射抑制材料因具有优良的低发射、辐射降温性能^[1],被认为是解决日益严重的热污染的有效方法。由 Stefan-Boltzmann 定律^[2]可知,降低材料表面发射率是有效抑制红外辐射的必要条件。当前,常见的低红外发射率材料通过载流子迁移、薄膜反射等手段实现红外辐射管理。例如:光子晶体^[3-5]利用周期排列形成的光子禁带调控热辐射光谱,将禁带区域扩宽至所需波段,实现红外高反射;掺杂氧化物半导体^[6-8]通过调控载流子浓度和碰撞频率,调节材料红外发射率,使其具有较低的红外吸收。

超材料(MM)是红外辐射抑制材料的一个新兴分支,通过调整其图案形状及结构参数可精确控制红外发射带宽及位置,其具有高度灵活的光谱调控能力和光谱可设计性^[9],可实现红外发射光谱选择性调控^[10]。近年来,基于超材料的热管理器件表现出优异的红外辐射抑制效果^[11]。Huang 等^[12]提出了一种多光谱兼容超材料,实现了低红外发射率($\epsilon_{8-14\ \mu\text{m}}=0.17$),避免了外部红外源的存在,减弱了设备自身发热。Zhu 等^[13]制备了一种多层超材料结构,其可用于可见光、中远红外($\epsilon_{3-5\ \mu\text{m}}=0.11$ 和 $\epsilon_{8-14\ \mu\text{m}}=0.12$)、激光和微波多光谱伪装,在非大气窗口($\epsilon_{5-8\ \mu\text{m}}=0.61$)进行辐射冷却,可承受至少 $300\ \text{C}$ 的温度。An 等^[14]提出了一种高强度隔热骨架和低发射率红外超材料双重调节方案,低隔热性[约 $0.104\ \text{W}/(\text{m}\cdot\text{K})$]和低红外发射率($800\ \text{C}$ 时

约 0.39)可使目标红外的辐射能量降低 91.7% 。由此可见,基于超材料的光谱选择性调控对于实现红外辐射抑制效果具有重要意义。然而,受限于仿真软件的计算资源和算力,研究人员难以计算毫米级超材料的红外光谱响应,仅通过实验手段研究其算术平均近似发射率不利于红外辐射抑制材料的进一步发展。因此,迫切需要开发一种计算毫米级超材料红外光谱响应的模型^[15-16]。

本文提出了一种毫米级方形超材料红外光谱响应的计算模型,并结合电场散射效应分析了毫米方形图案的边缘电场分布对红外反射率的影响。通过全波电磁仿真软件 FDTD 和参数扫描法研究了 Au 和 SiO_2 厚度对红外光谱响应的影响,确定了超材料红外反射层和基底层的最优厚度。基于此,设计了两种相同占空比、不同单元周期的方形超材料,将该目标离散化为顶点、边、连续介质等独立的求解单元。然后采用 FDTD 软件在不同边界条件下对其逐个进行求解及加权叠加,获得了毫米级方形超材料在红外微米波段内的反射光谱和电场分布,验证了电场散射效应对中远红外波段光谱响应的影响。随着单元尺寸和间隔的减小,超材料的红外反射光谱上移,并在 $8\sim 10\ \mu\text{m}$ 远红外波段内表现出更优的红外辐射抑制性能。最后,本文还利用不锈钢掩模版,结合磁控溅射技术制备了所设计超材料的样品,通过傅里叶红外光谱仪测量了样品在 $2\sim 16\ \mu\text{m}$ 全红外波段内的反射光谱。测试结果和仿真结果较好地吻合。本文所提出的计算模型有效提高

收稿日期: 2023-08-24; 修回日期: 2023-09-26; 录用日期: 2023-11-30; 网络首发日期: 2023-12-10

基金项目: 国家自然科学基金(52304410, 51972242)、湖北省重大项目(2023BAA003)、湖北省青年拔尖人才培养计划

通信作者: *lixiangcheng@wust.edu.cn

了毫米级超材料红外反射器的设计效率,在多光谱兼容设计、辐射制冷、红外信号探测等领域具有广阔的应用前景。

2 设计与仿真

2.1 毫米级超材料红外发射光谱计算模型

目前,超材料的平均发射率 ϵ 由经验公式估算得到,其表达式如下:

$$\epsilon = \epsilon_m f_m + \epsilon_d (1 - f_m), \quad (1)$$

$$f_m = \frac{w^2}{p^2} = \frac{w^2}{(w + g)^2} = \left(\frac{1}{1 + g/w} \right)^2, \quad (2)$$

式中: ϵ_m 、 ϵ_d 分别表示红外超材料结构的金属层发射率

和介质层发射率; f_m 、 p 、 w 和 g 分别表示金属占空比、周期、边长和间隙。基于式(1)、(2),可粗略估算毫米级红外超材料的算数平均发射率。

随着信号探测技术的高速发展,超材料在光波、电磁波、声波等领域的兼容性应用备受关注。为了实现多频段选择性调控,针对超材料的频域响应模拟成为关键一环。然而,考虑到制备工艺和工程应用的因素,红外/雷达、红外/可见光/雷达兼容超材料的设计与制备基本维持在毫米级尺度,跨越多个数量级的超材料结构的频域响应无法直接通过仿真软件计算得到,求解毫米级模型红外光谱响应的问题尚未得到解决。为填补该空白,本文基于式(1)、(2)提出了一种毫米级方形超材料模型的红外发射光谱 ϵ^* 计算公式,其表达式如下:

$$\epsilon^* = \sum_{i=1}^j A_i \epsilon_i = \sum_{i=1}^4 (A_1 \epsilon_1 + A_2 \epsilon_2 + A_3 \epsilon_3 + A_4 \epsilon_4) = \left(\frac{4\Delta x \Delta y}{p^2} \right) \epsilon_1 + \left\{ \frac{2[\omega - 2(\Delta y/2)]\Delta x + 2[\omega - 2(\Delta x/2)]\Delta y}{p^2} \right\} \epsilon_2 + \left[\frac{(\omega - \Delta x)(\omega - \Delta y)}{p^2} \right] \epsilon_3 + \left[\frac{p^2 - (\omega + \Delta x/2)(\omega + \Delta y/2)}{p^2} \right] \epsilon_4, \quad (3)$$

式中: A_i 、 ϵ_i 分别表示毫米级超材料模型的不同区域面积占比和区域发射率, $i=1, 2, 3, 4$ 分别代表顶点、边、介质和中心区域。一旦确定其中微元区域 $\Delta x \Delta y$ (一般各取两个工作波长,且令 $\Delta x = \Delta y$),即可求得其余区域面积占比。接着,采用 FDTD 仿真软件计算各微元区域在 1~2 个工作波长内的发射率 ϵ_i , 结合式(3)即可求解毫米级超材料在微米工作频带内的红外发射率光谱,根据基尔霍夫定律求得其反射率光谱。

2.2 毫米级超材料厚度对红外反射率的影响

基于上述计算公式,本文提出一种毫米级红外超材料结构,选用高电导率材料金(Au)作为红外反射层,红外透明材料石英玻璃(SiO_2)作为基底。为了探究金属反射层和基底厚度对红外反射光谱的影响,采用 FDTD 对 Au、 SiO_2 进行全波数值模拟。在 x 和 y 方向采用周期边界条件、在 z 方向采用完美匹配层(PML)。Au^[17]、 SiO_2 ^[18] 的折射率 n 、消光系数 k 被导入 FDTD 材料库中进行拟合,得到各自光学介电常数的实部 ϵ' 和虚部 ϵ'' 如图 1 所示。

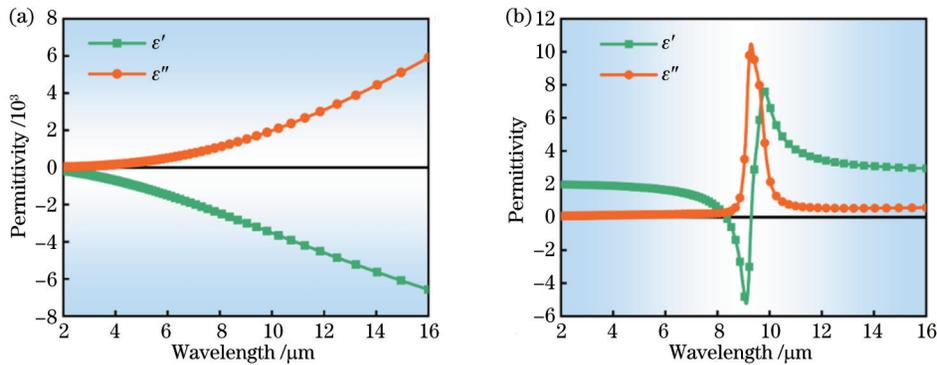


图 1 FDTD 拟合得到的红外介电常数。(a) Au; (b) SiO_2

Fig. 1 Infrared permittivity obtained by FDTD fitting. (a) Au; (b) SiO_2

根据图 1 中的光学介电常数模型,研究电磁波正入射至不同厚度薄膜的反射光谱,结果分别如图 2、3 所示。图 2 模拟了厚度为 0.05~5 μm 的 Au 膜红外反射光谱,图 3 模拟了厚度为 0.1~8 μm 的 SiO_2 基底红

外反射光谱。从图 2(a)可以看出: Au 膜的红外反射光谱随着厚度的增加向上移动。当 Au 膜厚度增至 0.08 μm 时,平均红外反射率为 98.6%; 当 Au 膜厚度增至 0.10 μm 后,结合图 2(b)可以发现,其红外反射光

谱逐渐趋于稳定,平均反射率约为 99%。从图 3(a)可以看出,当二氧化硅基底的厚度增加至 0.7 μm 时,其 2~8 μm 、12~16 μm 内的平均反射率低于 10%,而 8~10 μm 区域内出现异常高反射,最高可达 50%。从图 3

(b)可以发现,随着厚度的持续增加,二氧化硅基底的红外反射率在 8~11 μm 内保持在 70% 左右,其余波段具有良好的低红外反射特性。

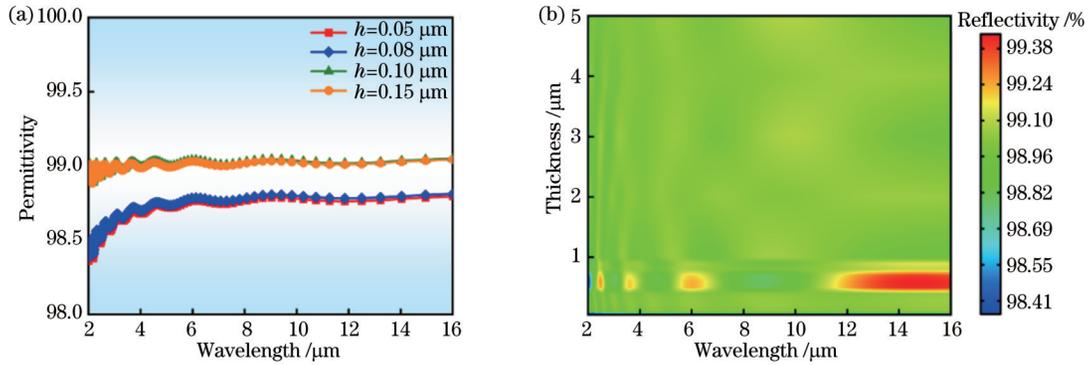


图 2 不同厚度的 Au 薄膜红外反射光谱仿真结果。(a) 0.05~0.15 μm ; (b) 0.15~5 μm

Fig. 2 Simulated results of infrared reflectance spectra of Au thin films with different thicknesses. (a) 0.05-0.15 μm ; (b) 0.15-5 μm

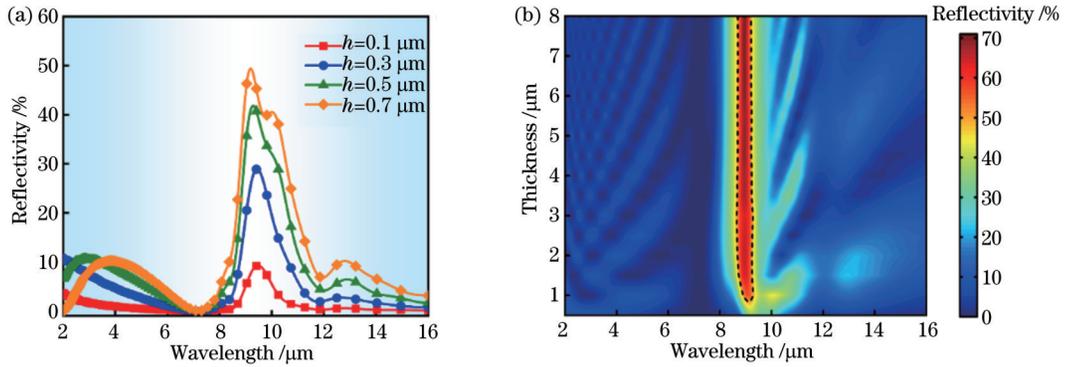


图 3 不同厚度 SiO₂ 薄膜的红外反射光谱仿真结果。(a) 0.1~0.7 μm ; (b) 0.1~5 μm

Fig. 3 Simulated results of infrared reflectance spectra of SiO₂ thin films with different thicknesses. (a) 0.1-0.7 μm ; (b) 0.1-5 μm

2.3 毫米级超材料结构与红外反射光谱仿真计算

上述研究结果验证了调节厚度可以影响红外反射率的变化,从而导致吸收强度和谐振带宽的变化,由此可确定仿真金反射层厚度为 0.1 μm ,同时选择二氧化硅玻璃作为基底。另外,方形贴片具有优良的

可加工性和较大的占空比,利于提高红外反射率,故本文设计了两个相同占空比(81%)、不同尺寸的 Au 方形超材料 MM1 和 MM2 模型,MM1 的边长、单元间隔分别为 $w_1=0.45 \text{ mm}$ 、 $g_1=0.05 \text{ mm}$,MM2 的边长、单元间隔分别为 $w_2=0.90 \text{ mm}$ 、 $g_2=0.10 \text{ mm}$,如图 4 (a)所示。

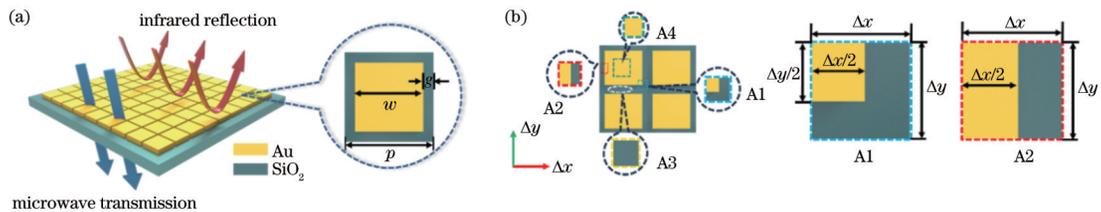


图 4 大尺寸 Au 超材料结构。(a) 结构示意图; (b) 仿真模型

Fig. 4 Large-scale Au metamaterial structure. (a) Structural diagram; (b) simulation model

基于 2.1 节提出的毫米级超材料的红外发射光谱计算模型,在 FDTD 仿真软件中将顶层 Au 和玻璃基底构成的方形超材料分为 4 个区域(A1~A4),如图 4 (b)所示。其中, Δx 、 Δy 同时取 $2\lambda = 32 \mu\text{m}$,将 A1 区域

在 x 、 y 方向的边界条件设置为 PML,将 A2 区域在 x 、 y 方向的边界条件分别设置为 PML、periodic,并且将光源设置在距离顶层一个波长的位置,仿真得到各区域的红外反射光谱如图 5(a)所示。

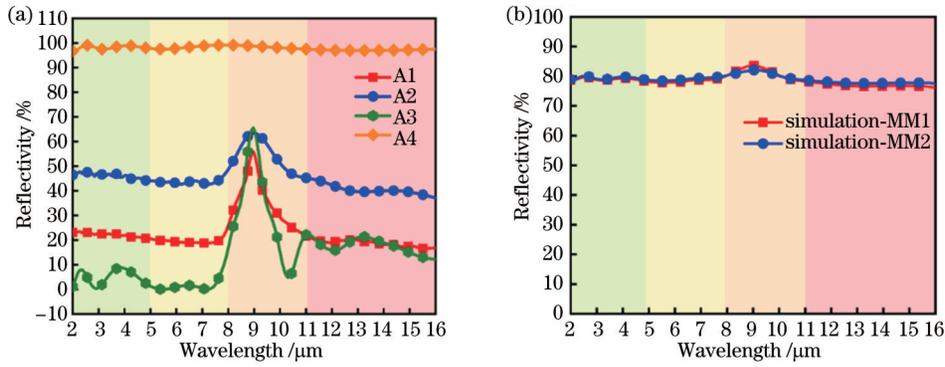


图5 红外反射光谱的仿真结果。(a)A1~A4;(b)MM1和MM2

Fig. 5 Simulated results of infrared reflectance spectra. (a) A1-A4; (b) MM1 and MM2

从图5(a)中可以发现,顶点A1区域、边A2区域的红外反射光谱在8~11 μm范围内均出现了“针尖”强谐振峰,其趋势几乎与介质A3区域(SiO₂)高度相似,这说明顶点区域及边缘区域对电磁场的散射效应对超材料红外反射光谱具有不可忽略的影响。此外,A4区域可视为单层Au薄膜,其红外反射光谱与图2(a)基本一致。接着计算各区域的面积占比,将其与各自红外反射光谱代入式(3),通过计算可求得两种结构单元MM1和MM2整体的红外反射光谱,如图5(b)所示。可以看出,虽然二者的面积占比相同,计算得到的红外反射光谱趋势相似,且在2~16 μm红外波段内的反射率均接近80%,但其单元周期和间隔存在差异,边缘区域对电磁波的散射效应导致两种尺寸模型的红外反射谱幅值略微不同,即具有小尺寸

的MM1结构在8~10 μm内的红外反射光谱幅值略大,最大可达83.58%,而MM2结构的反射率峰值仅达到82.09%。

为解释上述现象产生的物理机制,图6模拟了Au方形超材料的A1顶点散射区域和A2边缘散射区域在8.8 μm处的电场分布。可以发现,电场主要集中于正方形图案的侧面边界,且在上下两个方向均发生散射。图6(a)表明顶点散射区的电场集中分布在Au层顶点的上下两端,而基底几乎无电场透过,导致红外反射能量增强;图6(b)表明边散射区的电场较为均匀地分布在Au层侧边,且靠近外侧的基底表面内部电场强度略微升高,导致部分红外光透过,但A1与A2整体向下散射的能量小于向上散射的能量,因此在该波长的红外反射率仍保持较高水平。

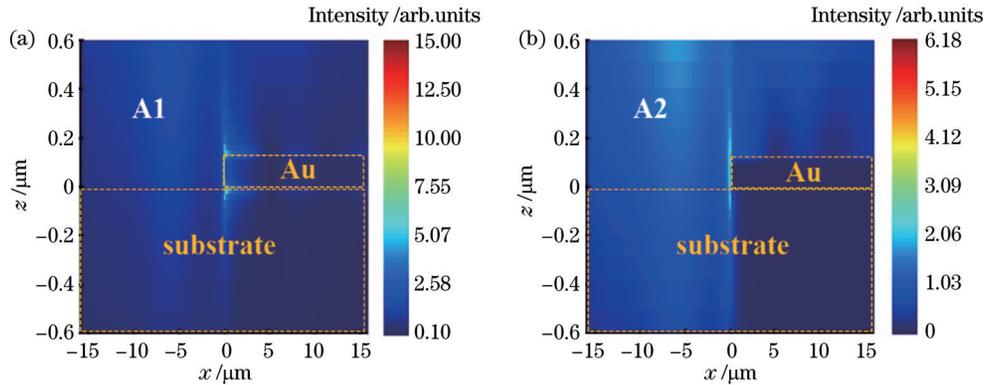


图6 波长8.8 μm处的电场分布。(a)A1顶点散射区;(b)A2边缘散射区

Fig. 6 Electric field distributions at 8.8 μm. (a) Vertex scattering region A1; (b) edge scattering region A2

综上,由于电磁场具有边缘效应,导电金属薄膜的边界处存在表面电流集中现象,导致正方形导电图案边缘处的电场散射情况与图案中心处的散射情况完全不同,尤其是正方形的顶点部分,尖锐的顶点会导致强烈的边缘散射。随着边长的减小,相同面积内的正方形数量会迅速增加,边缘散射效应会更加明显,从而导致小尺寸的MM1结构在8~10 μm内红外反射光谱幅值略高。

3 实验与验证

3.1 红外超材料制备与表征

为验证理论模型的计算结果,采用磁控溅射设备(FJL500)制备了两个超材料样品。选择玻璃作为衬底,将其分别在丙酮、乙醇、去离子水中超声清洗15 min,清洗过程有利于去除吸附的杂质。采用聚酰亚胺胶带将不锈钢掩模版固定在洁净玻璃衬底中心,随后移置于正对Au靶上方的样品台中央,打开功率

源,将真空腔室预抽真空至 1×10^{-4} Pa。在本文中,溅射过程均在室温(25 °C)下进行,Au的沉积速率为8 nm/min,沉积厚度约为100 nm,通过上述方法在玻璃基底上成功制备了两种尺寸的Au超材料(MM1、MM2)。

图7为仿真与测试结果。采用偏光显微镜(Axioskop40)拍摄得到MM1、MM2的光学图片,分别如图7(b)、(c)所示。可以明显观察到,通过磁控溅射制备的样品呈方形阵列规则排布,其图案整体区域大小为30 mm×30 mm,每个方形单元排列整齐,间隔较均匀。

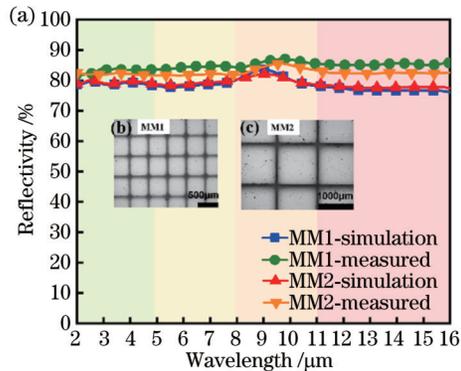


图7 仿真与测试结果。(a)反射光谱;光学显微镜拍摄的(b)MM1和(c)MM2

Fig. 7 Simulated and measured results. (a) Reflectance spectra; (b) MM1 and (c) MM2 captured by optical microscope

3.2 红外光谱响应分析

为研究超材料红外辐射抑制性能,本文使用FTIR(Spectrum-100)表征了MM1、MM2的红外反射率光谱(2~16 μm),并与仿真结果进行对比,如图7(a)所示。可以看出,FDTD模拟的红外反射光谱在8~10 μm内具有“针尖”反射峰,在实测红外反射光谱8.5~11 μm范围内同样出现了该现象。与仿真结果相比:实测得到的红外反射光谱向长波方向轻微红移,反射曲线向上移动,这是由于溅射过程中存在制备误差,激光刻蚀加工的掩模版无法克服倒角问题,导致测量结果与模拟结果存在略微差异。此外,对比MM1与MM2的实测结果可以发现:随着单元尺寸和间隔的减小,红外反射光谱逐渐上移,其中排列紧密的MM1表现出较好的红外反射性能;同时,计算MM1、MM2在2~16 μm内的平均反射率分别为78.59%和79.02%,而实测得到的平均反射率分别为84.78%和82.59%,理论数值与实际数值误差控制在5%左右,且红外反射光谱的整体趋势与规律基本吻合。以上结果表明,相同占空比下,小尺寸图案具有更高的红外反射率,同时验证了顶点、边区域的电磁散射效应对毫米级超材料红外光谱响应的影响不可忽略。

图8比较了本文设计的超材料结构与文献[15-16, 19-25]报道结构的红外辐射性能。可以看出,本

文通过磁控溅射技术和不锈钢掩模版制备的Au超材料样品具有低层数(1层)、超宽带(2~16 μm)、低发射率(<0.15)等优点,同时,本文利用FDTD计算出的毫米级超材料在中远红外范围内的光谱响应能够直观地反映特定波段内的红外辐射特性,毫米级超材料在多光谱兼容设计、辐射制冷、红外信号探测等领域具有广阔的应用前景。

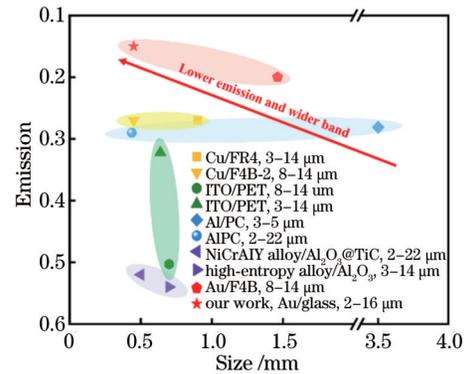


图8 红外发射率性能对比

Fig. 8 Infrared emissivity performance comparison

4 结 论

提出了一种毫米级超材料的红外光谱响应计算模型。通过对超材料红外反射特性进行仿真模拟和优化发现,当占空比相同时,单元周期减小导致超材料的边缘电场散射效应增强,这提升了远红外波段内的反射率。利用磁控溅射技术和不锈钢掩模版制备了Au方形超材料,当单元周期为0.5 mm时,所制备的超材料在2~16 μm中远红外波段范围内的反射率超过81.9%,在8~10 μm波长范围内反射率甚至达到了87.05%,表现出优异的红外辐射抑制特性。仿真与测试得到的红外反射光谱趋势较好地吻合。综上,本文所提出的计算模型可以针对设计需求,有效提高毫米级超材料红外反射器的设计效率,在宽带红外辐射抑制功能器件设计领域具有良好的应用前景。

参 考 文 献

- [1] 杜汐然, 王雪畅, 朱斌. 个人辐射制冷织物的研究进展[J]. 激光与光电子学进展, 2023, 60(13): 1316006.
Du X R, Wang X Y, Zhu B. Personal radiative cooling textile generation[J]. Laser & Optoelectronics Progress, 2023, 60(13): 1316006.
- [2] Feng X D, Pu M B, Zhang F, et al. Large-area low-cost multiscale-hierarchical metasurfaces for multispectral compatible camouflage of dual-band lasers, infrared and microwave[J]. Advanced Functional Materials, 2022, 32(36): 2205547.
- [3] Deng Z C, Su Y R, Qin W, et al. Nanostructured Ge/ZnS films for multispectral camouflage with low visibility and low thermal emission[J]. ACS Applied Nano Materials, 2022, 5(4): 5119-5127.
- [4] 李嘉威, 李享成, 陈平安, 等. 基于能带结构特性Si/ZnO多层膜的设计与制备[J]. 光学学报, 2023, 43(9): 0931002.
Li J W, Li X C, Chen P A, et al. Design and fabrication of Si/

- ZnO multilayer films based on energy band structure characteristics[J]. *Acta Optica Sinica*, 2023, 43(9): 0931002.
- [5] 汤道麟, 李享成, 陈平安, 等. 中远红外超宽波段高反射一维光子晶体薄膜结构设计[J]. *硅酸盐学报*, 2022, 50(5): 1310-1315.
- Tang D L, Li X C, Chen P A, et al. Design of one-dimensional photonic crystal film structure with high reflection in ultra-wide range of mid-/ far-infrared band[J]. *Journal of the Chinese Ceramic Society*, 2022, 50(5): 1310-1315.
- [6] Cinali M B, Coşkun Ö D. Optimization of physical properties of sputtered silver films by change of deposition power for low emissivity applications[J]. *Journal of Alloys and Compounds*, 2021, 853: 157073.
- [7] Sun K W, Tang X F, Yang C L, et al. Preparation and performance of low-emissivity Al-doped ZnO films for energy-saving glass[J]. *Ceramics International*, 2018, 44(16): 19597-19602.
- [8] 叶志镇, 王凤志, 陈芳, 等. 宽禁带半导体光电材料及其应用研究[J]. *光学学报*, 2022, 42(17): 1716001.
- Ye Z Z, Wang F Z, Chen F, et al. Wide band gap semiconductor optoelectronic materials and their applications[J]. *Acta Optica Sinica*, 2022, 42(17): 1716001.
- [9] 王星儿, 许可, 范旭浩, 等. 基于选择性光谱响应结构的横向色散多焦点超透镜[J]. *中国激光*, 2023, 50(18): 1813014.
- Wang X E, Xu K, Fan X H, et al. Transversely dispersive multi-foci metalens based on selective spectral response structure [J]. *Chinese Journal of Lasers*, 2023, 50(18): 1813014.
- [10] Zhu R C, Wang J F, Jiang J M, et al. Machine-learning-empowered multispectral metafilm with reduced radar cross section, low infrared emissivity, and visible transparency[J]. *Photonics Research*, 2022, 10(5): 1146.
- [11] Yu K, Zhang W, Qian M D, et al. Multiband metamaterial emitters for infrared and laser compatible stealth with thermal management based on dissipative dielectrics[J]. *Photonics Research*, 2023, 11(2): 290.
- [12] Huang Y, Zhu Y N, Qin B, et al. Hierarchical visible-infrared-microwave scattering surfaces for multispectral camouflage[J]. *Nanophotonics*, 2022, 11(16): 3613-3622.
- [13] Zhu H Z, Li Q, Tao C N, et al. Multispectral camouflage for infrared, visible, lasers and microwave with radiative cooling[J]. *Nature Communications*, 2021, 12: 1805.
- [14] An Z M, Huang Y X, Zhang R B. High-temperature multispectral stealth metastructure from the microwave-infrared compatible design[J]. *Composites Part B: Engineering*, 2023, 259: 110737.
- [15] Li H Y, Yuan H, Costa F, et al. Optically transparent water-based wideband switchable radar absorber/reflector with low infrared radiation characteristics[J]. *Optics Express*, 2021, 29(26): 42863-42875.
- [16] Pang Y Q, Li Y F, Yan M B, et al. Hybrid metasurfaces for microwave reflection and infrared emission reduction[J]. *Optics Express*, 2018, 26(9): 11950-11958.
- [17] Ciesielski A, Skowronski L, Trzcinski M, et al. Evidence of germanium segregation in gold thin films[J]. *Surface Science*, 2018, 674: 73-78.
- [18] Li J C, Liu S, Wu S L, et al. Metamaterials-based broadband absorption in long-wave infrared frequency enabled by multilayered ENZ films on metal-coated patterned silicon[J]. *Optics Express*, 2023, 31(5): 8453-8464.
- [19] Zhong S M, Jiang W, Xu P P, et al. A radar-infrared bi-stealth structure based on metasurfaces[J]. *Applied Physics Letters*, 2017, 110(6): 063502.
- [20] Kang J F, Jing H H, Song C W, et al. Research on multifunctional integrated multispectral stealthy metasurface absorbers for infrared and radar[J]. *Infrared Physics & Technology*, 2023, 131: 104665.
- [21] Wen K H, Han T C, Lu H P, et al. Experimental demonstration of an ultra-thin radar-infrared bi-stealth rasorber [J]. *Optics Express*, 2021, 29(6): 8872-8879.
- [22] Duan Y P, Lei H, Huang L X, et al. Metasurface-based hierarchical structures: excellent electromagnetic wave absorbers with low-infrared emissivity layer[J]. *Advanced Engineering Materials*, 2022, 24(9): 2200127.
- [23] Gui B H, Wang J, Zhu Y, et al. High temperature infrared-radar compatible stealthy metamaterial based on an ultrathin high-entropy alloy[J]. *Optics Express*, 2022, 30(25): 45426-45435.
- [24] Zhu Y, Zhang L, Wang J, et al. Microwave-infrared compatible stealth via high-temperature frequency selective surface upon Al₂O₃-TiC coating[J]. *Journal of Alloys and Compounds*, 2022, 920: 165977.
- [25] Zhang T, Duan Y P, Liu J Y, et al. Asymmetric electric field distribution enhanced hierarchical metamaterials for radar-infrared compatible camouflage[J]. *Journal of Materials Science & Technology*, 2023, 146: 10-18.

Design and Fabrication of Millimeter-Scale Au Metamaterials with Infrared Radiation Suppression

Li Chenxi, Li Xiangcheng*, Chen Ping'an, Zhu Yingli, Zhu Boquan

State Key Laboratory of Refractories and Metallurgy, Wuhan University of Science and Technology, Wuhan 430081, Hubei, China

Abstract

Objective Using infrared radiation suppression materials is regarded as an effective method to address the worsening thermal pollution owing to their favorable low-emission and radiation-cooling properties. According to the Stefan-Boltzmann law, the reduction of the thermal surface emissivity of a material can effectively suppress the infrared radiant energy. Metamaterial (MM) is an emerging branch of infrared radiation suppression materials with highly flexible spectral modulation capability and spectral designability. The infrared emission bandwidth and position will be precisely regulated by adjusting their pattern shapes and structure parameters, and thus the selective modulation of the infrared emission

spectrum can be realized. However, due to the limitation of computer resources and computation power, it has always been challenging to directly obtain the infrared spectral response of millimeter-scale metamaterials through simulation software. Therefore, we hope to establish a computational model of the infrared spectral response of millimeter-scale metamaterials, which provides a novel approach for the design of broadband infrared radiation suppression functional devices.

Methods In this paper, the mid- and far-infrared spectral response of millimeter-square metamaterials is simulated based on the time-domain finite-difference method. Combined with the electric field scattering effect, the impact of the marginal electric field strength distribution of the millimeter square pattern on the infrared reflectivity is analyzed. According to the traditional empirical formula, the computational model of the infrared spectral response of millimeter-square metamaterials is proposed. Using the full-wave electromagnetic simulation software FDTD and the parameter scanning method, the effects of the thicknesses of Au and SiO₂ on the infrared spectral response are investigated, and the optimal thicknesses of the reflector layer and the substrate layer are identified. Herein, two square metamaterials with the same filling ratio and different unit periods are designed. Then, this objective is discretized into independent solution units such as vertices, edges, and continuous media, while the x and y directions are set as PML and periodic boundary conditions, respectively. The infrared spectral response and electric field distribution of the millimeter-square metamaterial are obtained by iterative calculation and weighted superposition, and the influence of the electric field scattering effect on the spectral response in the mid- and far-infrared bands is verified. After that, the samples of the designed metamaterials are prepared in this paper by utilizing a stainless-steel mask plate and magnetron sputtering technology. In addition, the reflectance spectra of the samples in the full infrared band from 2 to 16 μm are measured using a Fourier transform infrared spectrometer.

Results and Discussions The simulation results in Fig. 5 show that the infrared reflectance spectral trends of the two models are nearly close within the 2–16 μm band. However, in the range of 8–10 μm , the amplitude of the infrared reflectance spectra of MM1 is larger than that of MM2, with a peak reflectance of up to 83.58%. To interpret the physical mechanism underlying the above phenomenon, the electric field intensity distribution in the marginal scattering region of the metamaterial is simulated at the reflectance peak of 8.8 μm in Fig. 6. Due to the variation of the unit period, the electric field scattering effect in the marginal region leads to a slight difference in the amplitude of the infrared reflection spectrum. To verify the theoretical reliability of the model and the practical infrared radiation suppression characteristics, the measured infrared reflection spectra are shown in Fig. 7. As the cell size reduces, MM1 exhibits higher infrared reflectance performance, verifying that the electric field scattering effect in the marginal region contributes significantly to the millimeter-scale metamaterial infrared spectral response. The error between the theoretical and practical values is approximately 5%. Finally, Fig. 8 compares the results of this work with relevant studies, demonstrating the advantages of lower layer number, wider bandwidth, and lower emission.

Conclusions A computational model of the infrared spectral response of millimeter-scale metamaterials is proposed to simulate the infrared reflectance spectra and electric field strength distribution of metamaterials. It can be found that when the filling ratio is identical, the decrease of the unit period leads to the enhancement of the marginal electric field scattering effect of the metamaterials, which improves their reflectance properties in the 8–10 μm long infrared wavelength band. Au square metamaterials are prepared using magnetron sputtering technology and stainless-steel mask plates. The reflectivity of the fabricated metamaterials exceeds 81.9% in the range of 2–16 μm middle and long infrared wavelength bands when the periodic cell is 0.5 mm. In addition, the infrared reflectivity even reaches 87.05% in the 8–10 μm wavelength range, which shows superior infrared radiation suppression properties of the sample. The infrared reflectance spectral trends obtained from the simulation and test are in good agreement. In conclusion, the computational model proposed in this paper effectively improves the design efficiency of millimeter-scale metamaterial infrared reflectors, which is promising in the field of broadband infrared radiation suppression functional device design.

Key words optical design; millimeter-scale metamaterials; electric field scattering effect; finite-difference time-domain method; mid- and far-infrared high reflection